Magnetic Holes Upstream of the Martian Bow Shock: MAVEN Observations

H. Madanian[1], J. S. Halekas[1], C. Mazelle[2], N. Omidi[3], J. R. Espley[4], D. L. Mitchell[5], J. P. McFadden[5]

[1]Department of Physics and Astronomy, University of Iowa, Iowa City, IA, USA.
[2]L'Institut de Recherche en Astrophysique et Planétologie, CNRS, Université de Toulouse, UPS, CNES, France.
[3]Solana Scientific Inc., Solana Beach, CA, USA.
[4]NASA Goddard Space Flight Center, Greenbelt, Maryland, USA
[5]Space Sciences Laboratory, University of California, Berkeley, California, USA.

Key Points:

- Linear and rotational magnetic holes are observed in the solar wind upstream of Mars
- Proton temperature anisotropy inside the holes increases while alpha particles remain mostly isotropic
- Pickup ions create an environment favorable for generation of mirror mode structures upstream of the bow shock

Corresponding author: Hadi Madanian, `hadi-madanian@uiowa.edu`

Abstract

Magnetic holes (MHs) are pressure-balanced structures characterized by distinct decreases in the interplanetary magnetic field (IMF) strength in otherwise unperturbed solar wind. In this paper we present an analysis of MHs upstream of the Martian bow shock based on three months of observations by the Mars Atmosphere and Volatile EvolutioN (MAVEN) spacecraft. Plasma properties within and around these structures as well as their shape characteristics are examined. We find an occurrence rate of around 2.1 events per day. About 48 percent of all events are of linear type with magnetic field rotation across the hole less than 10 degrees. We observe linear magnetic holes both as isolated events and as part of a train of magnetic holes. The proton temperature anisotropy inside MHs increases while alpha particles remain mostly isotropic. The average electron temperature inside MHs modestly increases with increasing hole depth. The duration of linear holes at 1.5 AU shows an increase compared to durations at smaller heliocentric distances, but the structures remain asymmetrical and ellipsoid. A case study of MHs accompanied by a population of heavy pickup ions is also discussed.

Plain Language Summary

The solar wind, a supersonic flow of electrons and ions flowing radially outward from the Sun, carries a magnetic field. Magnetic holes are structures with reduced magnetic field strength that last between a few seconds to a few minutes. These structures have been observed at many places throughout the solar system. A common formation mechanism for magnetic holes is a wave mode instability that converts magnetic energy into ion thermal energy, known as the mirror mode. Mirror mode instabilities grow when the temperature of ions moving perpendicular to the magnetic field is higher than that of ions moving in the parallel direction. Mirror waves alter the magnetic field and the spatial structure of the plasma. In this paper, we use observations from the MAVEN spacecraft to study magnetic holes in the space environment around Mars.

1 Introduction

Solar wind magnetic holes (MHs) or magnetic decreases are structures characterized by distinct depressions in the interplanetary magnetic field (IMF) strength anticorrelated with plasma density variations (Turner et al., 1977; Tsurutani et al., 1992; Stevens & Kasper, 2007). MHs have been observed throughout the solar system at Mercury (Karlsson

et al., 2016), Venus (Zhang, Russell, Baumjohann, et al., 2008; Zhang, Russell, Zambelli, et al., 2008), 1 AU (Fitzenreiter & Burlaga, 1978; Chisham et al., 2000; Zurbuchen et al., 2001; Stevens & Kasper, 2007; Xiao et al., 2010; Balikhin et al., 2010), over a range of heliocentric distances (Burlaga et al., 2006, 2007; Fränz et al., 2000; Sperveslage et al., 2000; Winterhalter et al., 1995; Tsurutani et al., 2009) and solar latitudes (Fränz et al., 2000; Tsurutani et al., 2011; Winterhalter et al., 2000). Based on the rotation of the magnetic field across the structure, magnetic holes are classified as linear holes (when there is no or a small rotation), and rotational holes (for rotations greater than $\sim 30^{\circ}$). No definite argument against or in favor of a rotation angle limit has so far been proposed and different authors have chosen different angles to categorize linear MHs in their observations (e.g., rotations below 15° in Xiao et al. (2010), and below 5° in Fränz et al. (2000)). The rotational holes are associated with a current sheet and are considered a subset of directional discontinuities which do not require a field reduction (Smith, 1973).

Turner et al. (1977) estimated an occurrence rate of 1.5 per day for these structures at 1 AU. Through a multi-spacecraft analysis using Helios 1, 2 and Voyager 2 spacecraft data, Sperveslage et al. (2000) investigated the heliocentric radial dependence of MH occurrence rate between 0.3 AU and 17 AU. The occurrence rate remains constant within 1 AU, but decreases beyond 2 AU with increasing heliocentric distance, with no clear radial dependence observed between 1 and 2 AU. Out of 850 MHs in the Sperveslage et al. (2000) study, nearly 30% were linear holes, a rate much higher than the 13% rate observed in Ulysses data in the ecliptic plane (Tsurutani et al., 2009). Other studies at 1 AU have reported $\sim$39% of all magnetic holes are of linear type (Briand et al., 2010; Stevens & Kasper, 2007), while over the solar poles nearly half of the magnetic depressions are linear MHs (Fränz et al., 2000; Tsurutani et al., 2011). Both types of MHs have been observed at Venus. Zhang, Russell, Zambelli, et al. (2008) examined solar wind data from the Venus Express spacecraft for magnetic holes identified as the minimum field strength within a 300 s rolling window with at least 50% decrease below the background field, and found that at 0.72 AU the duration of rotational holes associated with a reconnection current sheet is generally less than 30 s and their thickness is about 2000 km, comparable to observations at 1 AU.

Magnetic holes occur in a variety of time scales from seconds to minutes (Fränz et al., 2000; Stevens & Kasper, 2007; Zurbuchen et al., 2001). These time scales correspond to tens of local proton gyroradii in spatial scale, which makes these structures kinetic-

scale phenomena. Several mechanisms have been proposed for the generation of MHs (or magnetic depressions). A substantial number of studies have considered the mirror mode instability as the likely formation mechanism of linear MHs (Tsurutani et al., 1992; Winterhalter et al., 1995; Stevens & Kasper, 2007; Burlaga et al., 2006). Mirror mode waves grow in high β (the ratio of the plasma thermal pressure to the magnetic pressure) plasma with temperature anisotropy $T_\perp/T_\parallel > 1$, where $\perp$ and $\parallel$ denote directions perpendicular and parallel to the background magnetic field, respectively. The temperature anisotropy serves as a source of free energy for particles to nonlinearly interact with magnetic field perturbations (Southwood & Kivelson, 1993; Tajiri, 1967; Hasegawa, 1969; Kivelson & Southwood, 1996). Mirror mode instabilities have been frequently observed in terrestrial and planetary magnetosheaths where shock compression and field line draping cause perpendicular ion heating that provides favorable conditions for mirror mode instabilities to develop (Califano et al., 2008; Erdős & Balogh, 1996; Hubert & Harvey, 2000; Joy et al., 2006; Lucek et al., 2001; Soucek et al., 2008; Tsurutani et al., 2011). Pickup ions produced through ionization of neutral particles in the extended planetary exosphere can also cause mirror instability in plasma. These ions are accelerated by the solar wind motional electric field perpendicular to IMF, introducing temperature anisotropy to the solar wind plasma (Szegö et al., 2000; Wu & Davidson, 1972). As such, pickup ions are considered the main source of mirror mode wave generation in the heliosheath and in cometary environments (Burlaga et al., 2007; Liu et al., 2007; Russell et al., 1987; Volwerk et al., 2016; Glassmeier et al., 1993). A comprehensive review by Tsurutani et al. (2011) described a classification scheme to distinguish mirror modes from magnetic decreases in which, mirror mode structures are considered quasi-periodic, while magnetic decreases are variable-scale and non-periodic features. In our study, the terms magnetic holes and magnetic depressions/decreases are used interchangeably. Other mechanisms for generation of MHs include, large-amplitude polarized Alfvenic waves (Buti et al., 2001), magnetic reconnection in the high corona (Zurbuchen et al., 2001), the ponderomotive force of phase steepened Alfven waves (Tsurutani et al., 2002), and dark solitons in the solar wind (Baumgärtel, 1999). In addition, an early theoretical kinetic framework developed by Lemaire and Burlaga (1976) aimed at explaining diamagnetic effects in the boundary layer of tangential discontinuities based on the kinetic properties of electrons and ions (Burlaga & Lemaire, 1978).

In this paper we aim to investigate magnetic holes upstream of Mars' bow shock at 1.5 AU and examine various characterizing plasma properties of these structures. We focus on small timescale magnetic depressions lasting less than a few minutes. The paper is structured as follows. In section 2 we describe the instrumentation and available data, in section 3 the event identification method is discussed, plasma conditions and variabilities of magnetic holes are presented in section 4, and in section 5 conclusions and implications are given.

2 Instrumentation and Data Processing

The MAVEN spacecraft was launched in November 2013 and was designed to measure the energy and particle input from the Sun into the Mars upper atmosphere (Jakosky et al., 2015). The spacecraft has an inclined elliptical orbit with a nominal altitude of 150 km at the periapsis, and 6220 km at the apoapsis. Each orbit is ∼4.5 hours and thanks to the orbital precession, observations cover a variety of local times, altitudes, and latitudes. Orbit properties changed slightly in Spring of 2019 (and still evolving) as the aerobraking phase of the mission started. All data used in this study are from level-2 calibrated data products. Magnetic field data are from the magnetometer system which consists of two fluxgate sensors mounted at two opposite ends of the solar arrays (Connerney et al., 2015). The sensors measure ambient magnetic field with a resolution of 0.008 nT and an accuracy of 0.05%. Magnetic field measurements have been averaged to a 1 s resolution. Ion measurements are from the Solar Wind Ion Analyzer (SWIA) instrument (Halekas et al., 2015). SWIA is an energy analyzer that measures ions with energies between 25 eV to 25 keV over a wide field-of-view (FOV) (360° azimuth × 90° polar) covered by 10 fine anodes, each 4.5° wide, in the solar wind direction plus 14 wider anodes, each 22.5°, covering the rest of the azimuthal plane. The polar angles (-45, +45) are swiped by electrostatic deflections, with 24 deflection steps at each energy bin, resulting in a 3.75° available resolution. Depending on the plasma environment and operation mode, SWIA returns data with different energy and angular resolutions. In the "fine " mode, 3D distributions are limited to energy bins and FOVs near the peak of the distribution. This is the default operation mode in the solar wind and has 7.5% × 3.75° × 4.5° energy and angular resolutions. In the "coarse " mode, distributions have smaller resolutions (15% × 22.5° × 22°) but cover almost all FOVs and energies. The time resolution of returned 3D distributions is 8 s. A set of ion moments (density, velocity, and temperature) is also

available that is calculated onboard from the current mode measurements. We use the fine mode data to derive ion moments for protons and alpha particles separately for higher accuracy. This is accomplished by estimating the ion energy at the peak of each distribution (i.e., proton energy), and dissecting the energy spectrum. To find moments in the magnetic field-aligned coordinates, the pressure tensor is first calculated in the instrument frame and then rotated into the magnetic field-aligned coordinates. This leads to two perpendicular terms in the diagonalized matrix of which, the higher term is adopted (for more details see section 2 in Halekas, Brain, et al. (2017)). The solar wind ion energy spectra at times may show ion populations below the nominal proton energy. These ions are associated with solar wind ions scattered from the SWIA instrument harnessing or spacecraft body, and most of them are excluded from the FOV and energy range in the fine mode and thus have negligible effects on our ion moment analysis. SWIA measurements are used in conjunction with the SupraThermal and Thermal Ion Composition (STATIC) instrument, an electrostatic analyzer combined with a time-of-flight module (McFadden et al., 2015). STATIC can resolve dominant ion species (H^+, He^+, He^{++}, O^+, O_2^+, CO_2^+) in the Martian atmosphere and magnetosphere. STATIC has a similar angular coverage to SWIA; however, its energy resolution in the solar is less. The 'c_6' data product of STATIC with 32 energy channels and 64 mass bins provides the most relevant data for our study. Distributions in this mode are summed over all FOVs. Electron density and temperature are measured by the Solar Wind Electron Analyzer (SWEA) instrument (Mitchell et al., 2016). SWEA is also an electrostatic analyzer that measures electrons in the 3 - 4600 eV energy range, with an energy resolution of $\Delta E/E \sim 17\%$. The temporal resolution of SWEA data is 2 s. SWEA data are corrected for the FOV blocking by the spacecraft body, background noise, and spacecraft potential that is usually slightly positive in the solar wind. Electron densities and temperatures are calculated from 1D moments by assuming an isotropic electron distribution.

3 Event Identification

We focused on three months of MAVEN observations between 1 June and 1 September 2016 when the MAVEN orbital apoapsis was on the dayside and precessed around the subsolar point, resulting in the spacecraft spending a substantial fraction of each orbit in the solar wind. We used a modeled bow shock boundary, a conic shape determined from an ensemble of Phobos 2 and Mars Global Surveyor data sets (Trotignon et al., 2006),

to identify solar wind segments of each orbit. An alternative way to select solar wind measurements would be to check a combination of criteria on the solar wind bulk flow velocity, ion temperature, and magnetic field fluctuations (Halekas, Ruhunusiri, et al., 2017). But since we are searching for field depressions that are isolated and have relatively large δB, that may not be the best approach for our purposes. To identify magnetic depressions we follow a similar method to Zhang, Russell, Baumjohann, et al. (2008) and Plaschke et al. (2018), with some modifications in the criteria to adapt them to MAVEN observations. We start with 1 Hz magnetic field data and calculate the depression time-series from $\Delta B/B = (B_i - B_{bg})/B_{bg}$, where B_i is the magnetic field magnitude at each point and B_{bg} (Background field) is the average magnetic field magnitude over a 150 s rolling interval. We scan the time-series, one point at a time, for minimum depressions within the rolling window. Once a minimum depression point is found, we check the following criteria: (1) $\Delta B/B$ should be less than $d_{th} = -0.35$, (2) one minute before and after the event, the standard deviation in magnetic field magnitudes, σ_B, should not exceed half of σ_B of the event interval, (3) the average magnetic field strengths one minute before and after the event should be within two standard deviations of one another; (4) the average plasma density, n, at the event time should not be less than one standard deviation of densities one minute before or after the event ($\bar{n}_{event} \geq \bar{n}_{before,after} - \sigma_{before,after}$).

An example of the search algorithm for a MH event on 15 August 2016 at 21:37:47 UTC is shown in Figure 1. In this figure, three components of the magnetic field in the Mars-centered Solar Orbital (MSO) coordinate are shown in panels (a)-(c). The MSO frame origin is at Mars $'$ center-of-mass with the $+X$ axis pointing to the Sun, the Z axis perpendicular to the ecliptic plane with $+Z$ pointing above the plane, and the Y axis completing the right-hand coordinate system (roughly anti-parallel to the Mars orbital velocity). The solid line in panel (d) represents the field strength, B, and the background field (B_{bg}) is shown with the dashed line. Panel (e) shows the depression time-series. The horizontal dashed-dotted line is drawn at -0.35, the depression threshold d_{th}. The two vertical dashed lines mark the start and end times determined as the nearest points to the minimum depression when the depression recovers and reaches $0.1 * d_{th}$.

The boundaries could also be identified as the nearest points with magnetic field magnitude larger than $B_{bg} - \sigma_B$, where σ_B is the standard deviation of magnetic field magnitude at event time. Both methods lead to identical boundaries for the majority

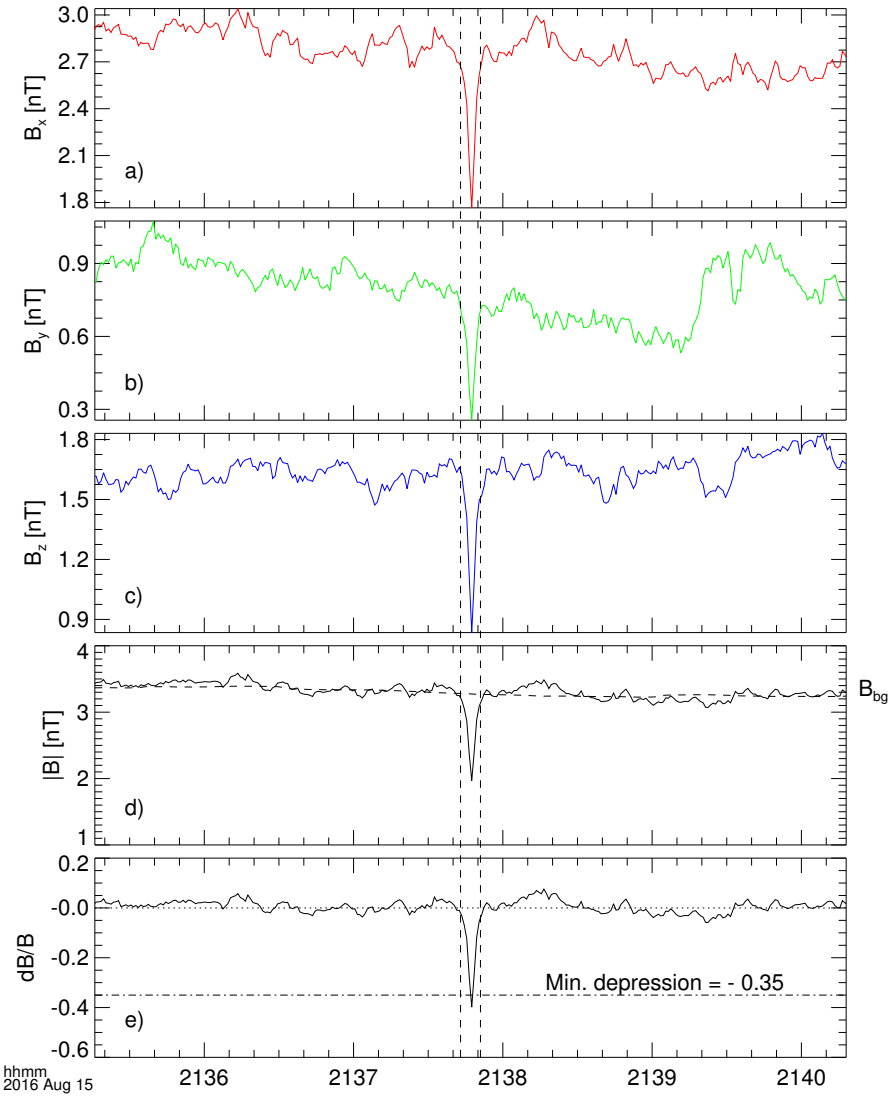

Figure 1. Magnetic hole event at 21:37:47 UTC on 15 August 2016. Panels (a)-(c) show the three components of the magnetic field in the MSO coordinate. The solid line in panel (d) shows the field strength B and the background field strength (B_{bg}) is indicated by the dashed line. B_{bg} is the averaged field strength over a 150 s window centered on the minimum depression point. Panel (e) shows the depression levels. The dashed dotted line at -0.35 is the minimum depression threshold (d_{th}). The two vertical dashed lines mark the the event boundaries determined when the depression reaches -0.035 (i.e. 10% of the threshold value).

of events, but for some events with asymmetrical field profiles around the minimum depression, setting a fixed threshold produced more precise boundaries.

The minimum depression threshold in criterion 1 is an empirical value, which provides adequate identification of MHs while minimizing false positive events. Reducing this threshold leads to more positive events, but at the expense of an increased risk of detecting random variations that are not MHs. Restricting σ_B before and after the event in criterion 2 increases the chance of selecting well-defined events. Criterion 3 eliminates step-like events, which commonly occur during shock crossings, foreshock compressional boundaries, and Short Large Amplitude Magnetic Structures (SLAMS) (Schwartz & Burgess, 1991; Omidi et al., 2009; Halekas, Ruhunusiri, et al., 2017). The main difference between our identification method and that of previous studies is criterion 4 which was implemented after finding many transient foreshock events in our initial event set. Hot Flow Anomalies (HFAs), Spontaneous HFAs, and foreshock cavities are among the foreshock transient structures that are characterized by correlated magnetic field strength and plasma abundance variations (Sibeck et al., 2004; Schwartz et al., 2006; Omidi et al., 2013; Omidi & Sibeck, 2007; Collinson et al., 2015, 2017). Some of these structures are associated with Ultra-low frequency (ULF) waves. As the solar wind interacts with a bow shock, some solar wind ions are reflected back upstream by the potential difference across the bow shock. The backstreaming ions move sunward in the solar wind frame with velocities in the order of a few Alfven speed and interact with the incident solar wind, driving nonlinear ion-ion instabilities that lead to generation of ULF waves (Gary et al., 1981; Hoppe & Russell, 1983; Halekas, Brain, et al., 2017; Mazelle et al., 1991; Gary, 1993). In addition, fluid models of the mirror mode instability have shown that energy exchange between parallel and perpendicular particle flux and field components drives the plasma out of the high magnetic field region and into the magnetic holes with decreased field causing increased plasma densities inside the holes (Southwood & Kivelson, 1993), which further supports inclusion of criterion 4. Stevens and Kasper (2007) classified magnetic holes found through this type of search algorithm as "young holes " which are near saturation and closer to the instability threshold. We performed the search with 300 s and 500 s windows to avoid any biases due to the shifting window size. Finally, events are visually inspected to ensure that all events are well-defined magnetic holes.

4 Observations

Figure 2 illustrates four examples of magnetic field profile across magnetic holes. Each event is presented within a 6-minute timespan. Panel (a) shows two magnetic holes

on 29 June 2016 separated by about one minute. The first depression at 04:50:55 UTC is more symmetric compared to the event at 04:52:00 UTC which possesses more structures in the middle (i.e., a nested hole). The second panel shows a MH at 20:54:36 UTC on 9 July, where recovery from the minimum depression occurs in two steps. There is also a smaller hole at around 20:53:25 UTC which does not meet the minimum depression requirement. These two events are also separated by about one minute. The magnetic field strength in the event on the third panel decreases by 84% and the structure is symmetrical, while the IMF surrounding the hole is very quiet.

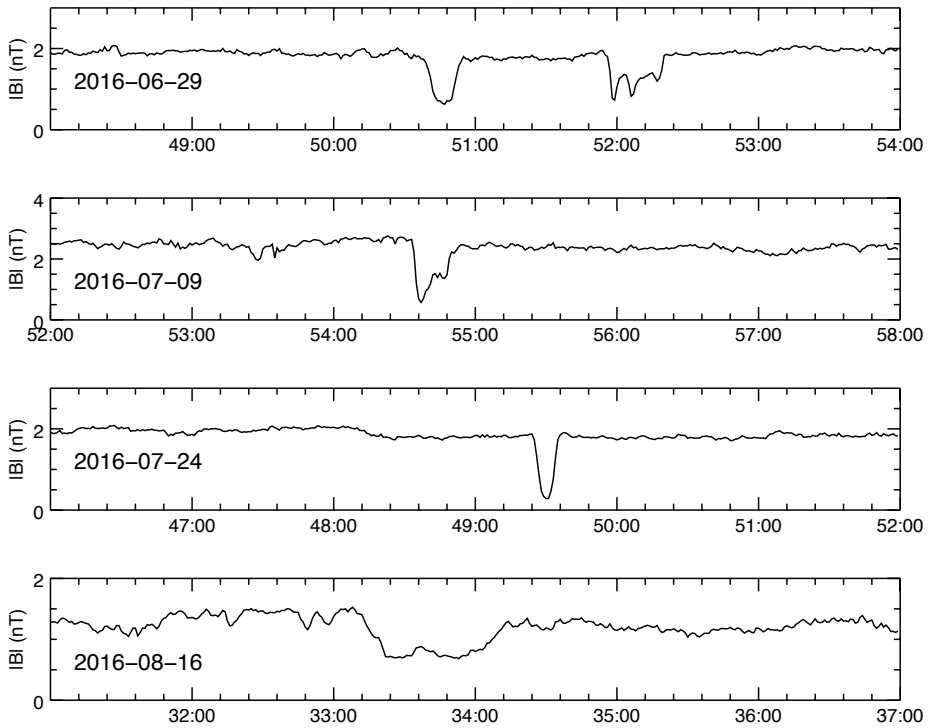

Figure 2. Four examples of magnetic field profile around MHs observed by MAVEN. Event dates are annotated on each panel. The horizontal axes indicate the UTC time.

The relatively long MH in the fourth panel occurred on 16 August 2016 between 15:33:10 and 15:34:12 UTC. The shape of this event is rather different than the previous examples. The boundaries are extended over a longer period and the depression is plateaued at around 0.7 nT and shows a peak near the center of the hole.

4.1 Statistical Analysis of Magnetic Holes

From three months of data used in our analysis we obtain 102 events which gives an occurrence rate of about 2.1 events per day considering that the spacecraft spent, on average, 55% of each orbit in the solar wind. The spatial distribution of events around Mars is shown in Figure 3 which illustrates a cylindrical projection of events. The axes are in units of Mars radii (R_M). Mars (in yellow) is at the origin and the meshed surface represents the modeled bow shock boundary. Events are spread along the spacecraft trajectory in the solar wind and do not show any particular pattern with respect to event duration, depth, or type. Some events appear very close to the bow shock, though they are still in the solar wind flow. For instance, for the event located on the boundary at $X_{SMO} \sim 1$ R_M the solar wind speed is ~490 km/s and the dynamic pressure ~2 nPa, which could displace the bow shock further inward than the model predicted.

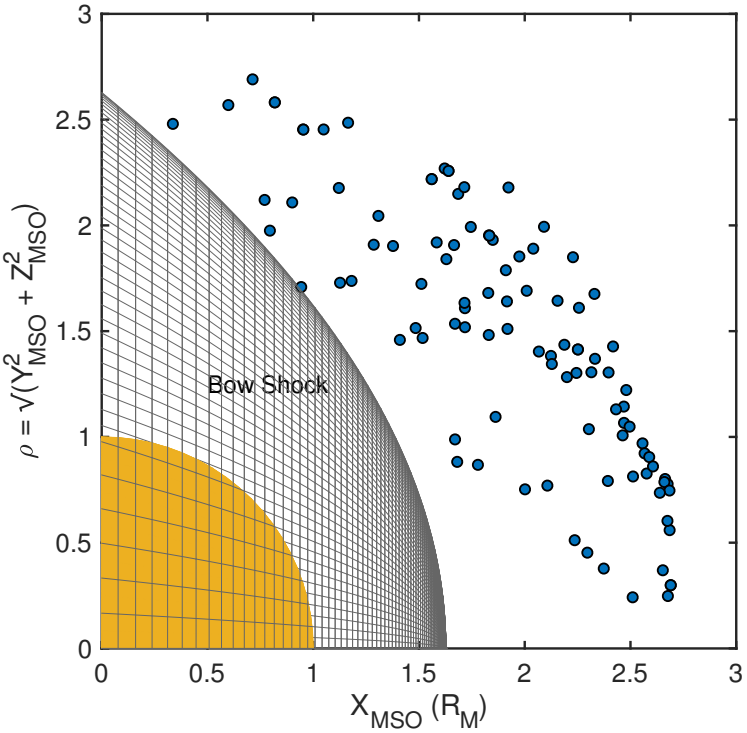

Figure 3. Distribution of magnetic holes upstream of the Martian bow shock in cylindrical coordinates. The axes are in units of Mars radii (R_M).

Once event boundaries have been determined, plasma parameters including, proton and alpha particle temperature, anisotropy, density, solar wind bulk flow speed, electron density and temperature during the event and in the adjacent solar wind are recorded.

We also calculate the magnetic field rotation, $\Delta\varphi$, across the holes using the magnetic field vectors at the start and end times. Panel (a) in Figure 4 shows the occurrence rate distribution of $\Delta\varphi$ which varies between 0.3° and 172°. The most probable rotation angle lies between 5° - 10°. Around ∼48% of events are linear MHs ($\Delta\varphi < 10°$). The event duration distribution in panel (b) shows an exponential decrease for events longer than 10 s. The median event duration is ∼19 s, and ∼15.5 s for linear holes. From event durations and the corresponding solar wind bulk flow velocity and proton temperature, we estimate the spatial scale size of events along the solar wind flow. Panel (c) in Figure 4 represents the scale size distribution per local proton gyroradii, r_ρ, calculated from the average magnetic field magnitude inside the holes. For rotational holes this size is a measure of the current sheet thickness. The distribution in panel (c) also shows an exponential pattern for structures larger than 15 r_ρ. Similar exponential distributions have been reported in previous statistical studies of MHs at 1 AU (Stevens & Kasper, 2007; Tsurutani et al., 2011).

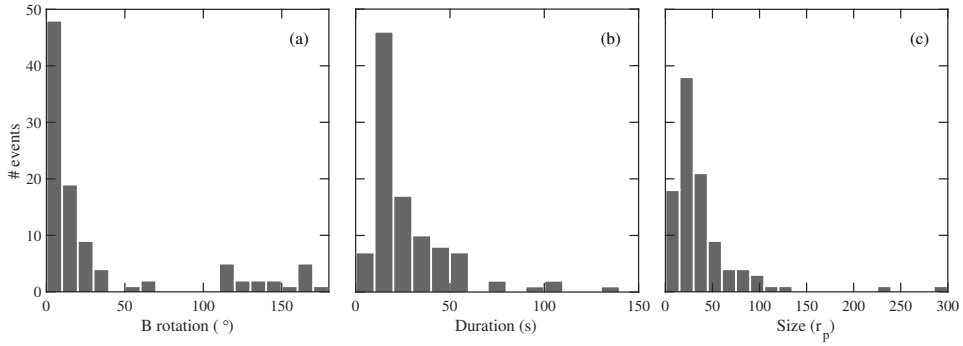

Figure 4. Occurrence rate distribution of (a) rotation of magnetic field across magnetic holes ($\Delta\varphi$), (b) event duration, (c) event size normalized in local proton gyroradii (r_ρ).

For linear magnetic holes the stability condition parameter R provides an estimate of whether mirror mode waves can develop in the plasma (Hasegawa, 1969; Winterhalter et al., 1994), and is defined by:

$$R = \frac{\frac{\beta_\perp}{\beta_\parallel}}{1 + \frac{1}{\beta_\perp}} \tag{1}$$

where $\beta_{\perp,\parallel}$ are the plasma betas calculated inside the holes,

$$\beta_{\perp,\parallel} = \frac{(n_p T_{p\perp,\parallel} + n_\alpha T_{\alpha\perp,\parallel})k_b}{B^2/2\mu_0} \tag{2}$$

n_p and n_α are the proton and alpha particle densities, respectively, k_b is the Boltzmann constant, μ_0 is the vacuum permeability constant, and T represents the corresponding ion temperatures. For $R > 1$, plasma is unstable and mirror mode waves can grow, while for values close to 1, plasma is considered marginally stable. The underlying particle distribution that drives this particular form of instability threshold is bi-Maxwellian. Non-Maxwellian distributions such as suprathermal ion tail, and anisotropic electron distributions both increase the pressure anisotropy and act to lower the instability threshold (Pokhotelov, 2002). The distribution histogram in Figure 5 shows the distribution of the highest instability parameter value for linear holes. The majority of the 49 linear holes are either unstable or only marginally stable (31 events show $R > 1$).

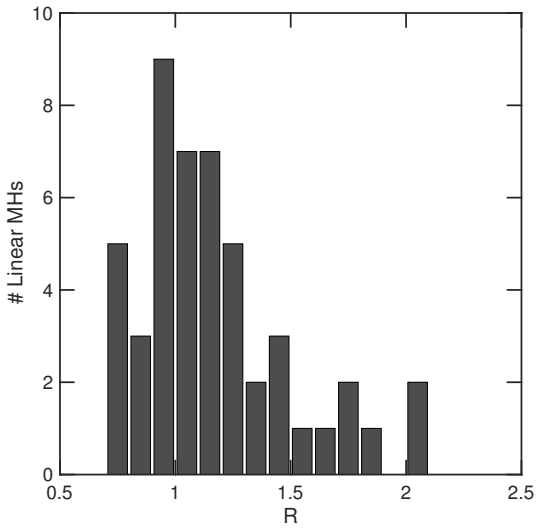

Figure 5. Histogram distribution of instability condition R for linear MHs with $\Delta\varphi < 10°$.

The solar wind proton perpendicular temperature inside the magnetic holes increases from its value in the ambient solar wind (Fränz et al., 2000; Neugebauer et al., 2001; Tsurutani, 2002). In panels (a) and (b) of Figure 6 we show histograms of inside-to-outside ratios of solar wind ion temperature perpendicular and along the local magnetic field, respectively. All 102 events are included in this figure. Proton temperature variations (blue bars) predominantly occur in perpendicular direction. Most events exhibit higher perpendicular proton temperature inside the hole, confirming the findings of previous

studies. The parallel temperature of protons also increases, but to a lesser degree. For alpha particles (red bars) the distributions are relatively symmetric, indicating that the alpha particles remain mostly isotropic.

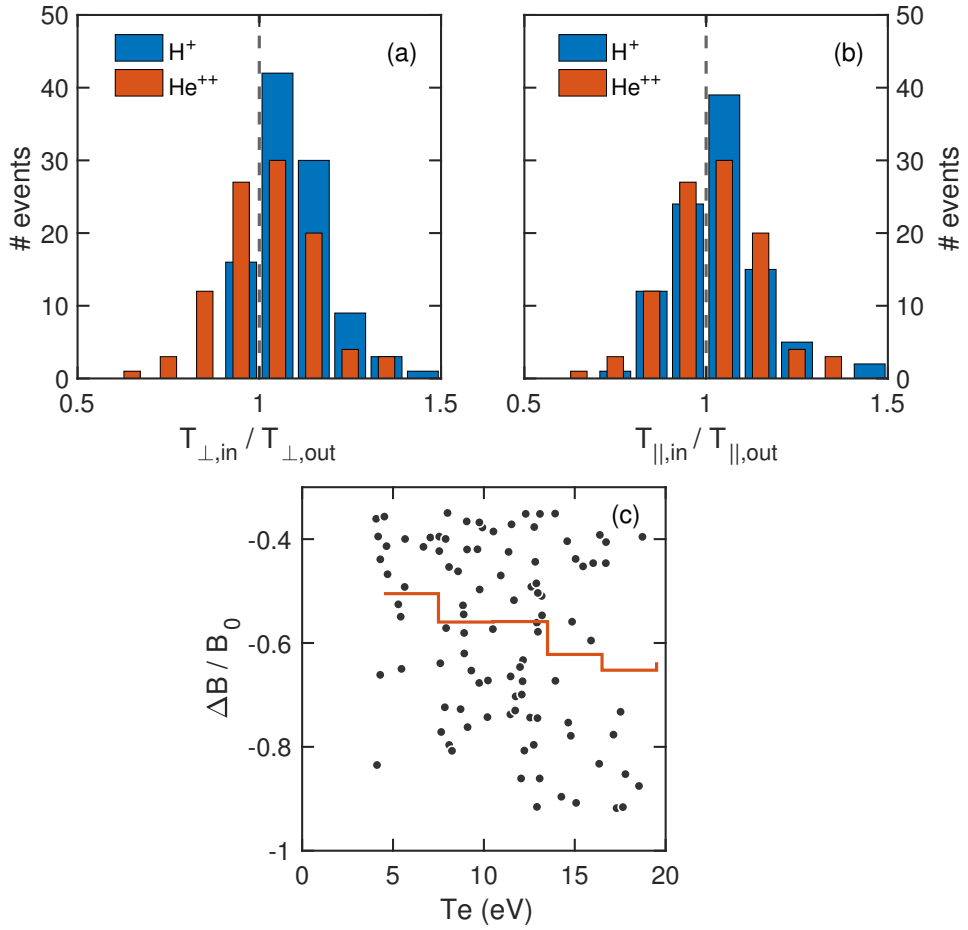

Figure 6. (a) Histogram of inside-to-outside ratios of solar wind protons (blue) and alpha particles (red) perpendicular temperature, (b) histogram of parallel temperature ratios, (c) distribution of event depressions as a function of electron temperature inside the holes. The red lines on panels(c) shows average depression depths in 3 eV temperature bins.

The hole depth ($\Delta B/B_{bg}$) distribution as a function of electron temperature is shown in panel (c) of Figure 6. The red line on this panel represents the averaged depths in 3 eV temperature bins. The electron temperature shows a modest increasing trend at higher magnetic depressions. Note that our assumption here is that electrons inside MHs are isotropic ($T_{e\perp} \approx T_{e\parallel}$) (Balikhin et al., 2012; Briand et al., 2010).

MHs associated with mirror mode instabilities are non-propagating in the plasma frame, and structures are extended along the background magnetic field. It has been shown that a typical magnetic hole at 0.72 AU has an asymmetrical shape in the form of a rotational ellipsoid with major to minor axes ratio of 2.45:1 (Zhang, Russell, Baumjohann, et al., 2008). A separate analysis at 1 AU showed a consistent shape with the elongation ratio of 1.84:1, suggesting that MHs develop inside 0.72 AU and their shape is preserved in the solar wind (Xiao et al., 2010; Ala-Lahti et al., 2018; Baumgärtel, 1999). While Burlaga et al. (2007) showed that the normalized size of MHs in the heliosheath is of the same order of magnitude as their size at 1 AU.

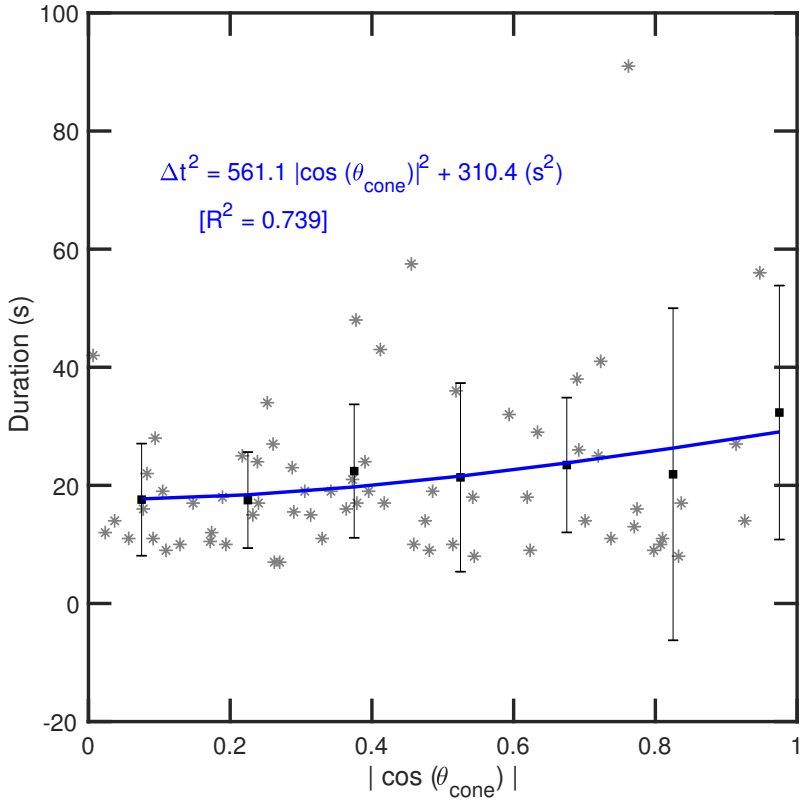

Figure 7. Magnetic hole duration as a function of background field orientation with respect to the solar wind flow. Only holes with $\Delta\varphi < 20^\circ$ are shown. Black squares show average values of the binned data. The blue line is the best fit on the squares describing the shape of a typical structure. The best fit function and the R^2 goodness-of-fit value are annotated in blue. Error bars indicate 1 standard deviation.

These observations suggest that there is a consistency in the shape of MHs throughout the interplanetary medium. Here, we attempt to estimate the typical shape of MHs at

1.5 AU using MAVEN data. Figure 7 shows MH durations as a function of IMF orientation with respect to the solar wind flow (i.e., $cos(\theta_{cone})$, where θ_{cone} is the IMF cone angle at the beginning of each event). In this figure, asterisks represent 68 MH events with magnetic field rotation $\Delta\varphi < 20°$, black squares show average durations of data in $0.15*|cos(\theta_{cone})|$ bins with error bars indicating 1 standard deviation, and the blue curve shows a hyperbola fit on the squares in the form of $\Delta t^2 = 561.1|cos(\theta_{cone})|^2 + 310.3$ (s^2). The goodness-of-fit is 0.739. From this equation, two characteristic times for magnetic field fully radial ($|cos(\theta_{cone})| = 1$) and fully perpendicular to the flow ($|cos(\theta_{cone})| = 0$) are estimated that show the typical dwell time for the spacecraft inside linear magnetic holes at 1.5 AU are ∼29.5 s along, and 17.6 s across the magnetic field. At 1.5 AU, the ratio of structure scale size along and across the magnetic field is about 1.67 (1.43 - 1.75):1.

4.2 Train of Magnetic Holes in the Solar Wind

Linear MHs are observed both as part of trains of holes or as isolated single events. Figure 8 shows an example of a train of MHs. Panel (a) in this figure shows the ion energy spectrogram from SWIA 3D coarse distributions between 100 eV – 7000 eV. The color bar represents the energy flux in logarithmic scale. The solar wind proton and alpha particle beams are recognizable at ∼850 eV and 1700 eV, respectively. Ion fluxes below the proton energy are associated with scattered solar wind ions (see section 2). Panel (b) shows magnetic field data in the MSO frame. Panel (c) shows the plasma density with an average proton density of ∼3.8 cm^{-3}. The proton temperature shows fluctuations between 5 – 6.5 eV, though no clear relation with magnetic field fluctuations is observed. Protons show a consistent temperature anisotropy at ∼1.5 in panel (e), while alpha particles (not shown) remain roughly isotropic. The instability parameter R in panel (f) is greater than 1 for the entire period. It seems that for magnetic hole trains the plasma is consistently unstable both inside and outside the depressions. All MHs in Figure 8 are linear. Linear MHs generated by mirror mode waves are stretched along the field line. To check the variations in the magnetic field frame, we performed the minimum variance analysis (MVA) on the magnetic field data. Panel (g) on this figure shows the principal magnetic field components B_1, B_2, and B_3 along the maximum (orange), intermediate (cyan), and minimum (black) variance vectors. The ratio of intermediate to minimum eigenvalues is about 3.4 and the maximum to intermediate ratio is greater than 8, which

indicate that the MVA is well conditioned. The maximum variance vector B_1 maintains the most variations, thereby the magnetic field varies primarily in one direction. The horizontal axis labels at the bottom represent altitude in units of km, surface latitude, surface longitude, and time (hh:mm), respectively. An important signature for the identification of mirror mode structures is an anticorrelation between the magnetic field strength and plasma density (Stevens & Kasper, 2007). We observe this anticorrelation in almost all holes (vertical dashed lines).

Mirror mode instabilities can also create magnetic peaks, characterized by local enhancements of magnetic field strength and decreased plasma density. Numerical simulations have shown that in the initial stages of their nonlinear evolution, mirror mode waves primarily give rise to magnetic peaks which eventually, after saturation and as plasma approaches a marginally stable condition, convert to magnetic holes/dips (Hellinger et al., 2009; Ahmadi et al., 2017). Other studies suggest that mirror mode waves generate magnetic holes and peaks but only magnetic holes survive as soliton structures (Baumgärtel, 1999). The magnetic peaks in Figure 8 (marked with vertical dotted lines) have smaller amplitudes than the holes and their corresponding density decrease is also small. Also note that due to low time resolution of SWIA data, density measurements exactly inside some structures may be missing (e.g., for the depression on the second dashed line at around 12:34:10 UTC). The spatial structure of the magnetic field in the second panel of Figure 8 is most likely caused by a nonlinear saturation mechanism.

Although quasi-periodic depressions in panel (b) are clearly caused by mirror mode waves, not all of the components of the magnetic field approach zero at each depression, which is used as an event identification criterion by some authors (e.g., Russell et al. (2008)). At each depression there is a component of the magnetic field, in both MSO and MVA frames, that does not approach zero and sometimes increases.

4.3 Isolated Magnetic Holes in the Solar Wind

In Figure 9 MAVEN observations of an isolated linear MH in the solar wind are shown. The hole is 13 s long and the field depression is ∼84%. All three components of the magnetic field are negative at this time and the solar wind flow speed is ∼432 km/s and remains unchanged throughout the event. Inside the hole, the proton density and temperature increase by about 33 and 25 percent, respectively. Temperature increase for

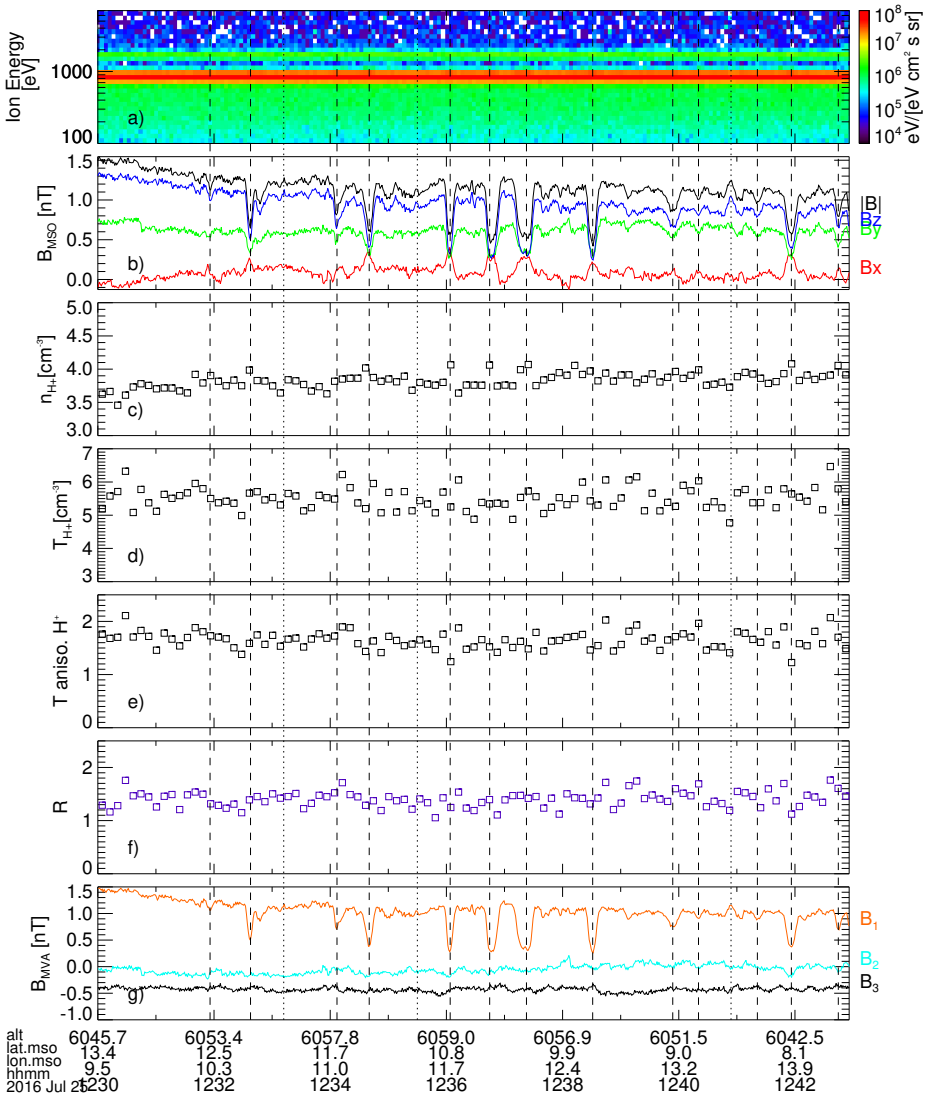

Figure 8. A train of magnetic holes in the solar wind on 25 July 2016 between 12:30:00 - 12:43:00 UTC. Panels show: (a) Ion energy spectrogram, (b) magnetic field components and magnitude in MSO coordinates, (c) proton density, (d) average proton temperature, (e) proton temperature anisotropy, (f) instability condition parameter, (g) magnetic field principal variance components. The vertical dashed and dotted lines indicate the instances of magnetic holes and peaks, respectively.

this event is much more noticeable than that observed for the train of holes in Figure 8. Solar wind protons and alpha particles are fairly isotropic except inside the depression where both anisotropies increase to above 1.5. We discussed in section 4.2 that solar wind plasma carrying a train of MHs is unstable to the mirror mode instability through-

out the entire structure. Our observations suggests that the plasma around isolated MHs becomes marginally stable or unstable only near and within the depression and it departs from the instability condition at other times.

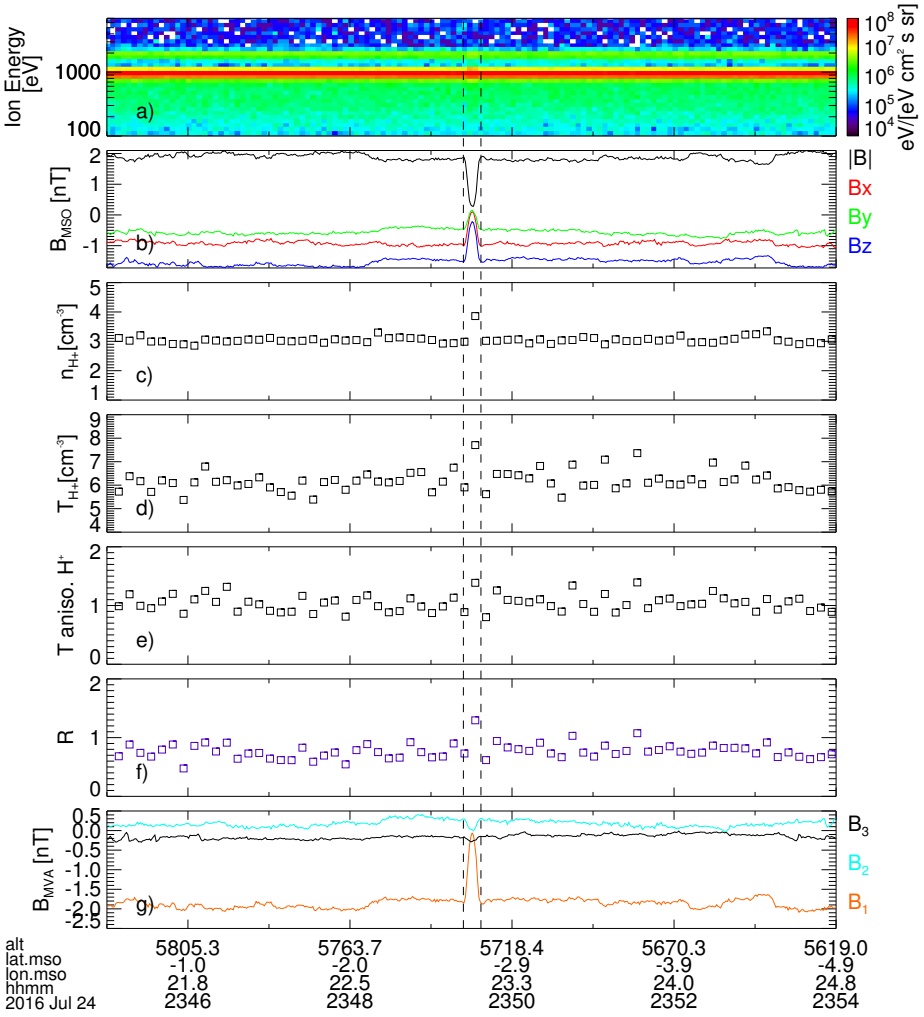

Figure 9. Similar to Figure 8 but for an isolated event on 24 July 2016. The vertical dashed lines mark the boundaries of the MH.

4.4 Magnetic Holes in the Extended Martian Exosphere

In this section, properties of MHs upstream of Mars in the presence of pickup ions are examined and main differences to MHs observed in the "pure" solar wind are identified. An interesting feature that differentiates studying MHs at Mars from other places in the solar system is the extended Martian exosphere and pickup ions that are contin-

uously introduced in the upstream solar wind. The neutral species are normally bound by Mars' gravity unless they acquire enough escape energy that enables them to travel upstream (for comprehensive reviews of this topic readers are referred to reviews by e.g., Lammer et al. (2008); Brain et al. (2016) and references therein). Pickup ions, mainly atomic oxygen and hydrogen ions, can be generated over a long distance upstream of the bow shock, extent of which is determined by the escape velocity of the neutral species. These ions gyrate around the IMF and form a ring-beam in the velocity distribution function (VDF). Depending on the distance to Mars at the time of creation and local solar wind conditions, pickup ions can be energized to values well above the incident solar wind energy and drive significant temperature anisotropy. Figure 10 shows examples of linear MHs occurring in the presence of high fluxes of heavy pickup ions on 27 August 2016 between 12:50:00 - 13:00:00 UTC. During this time, the spacecraft had just crossed the terminator plane on dawn side above the northern hemisphere. Heavy pickup ions (O^+) are distinguishable in the energy spectrogram of panel (a) at energies around and above 10 keV. These ions are in an early stage of their gyration. Panel (b) shows the azimuthal angle coverage of the SWIA FOV in the coarse mode. The solar wind signal is evident in $150° - 200°$ phi angles. The flux of non-solar wind ions in $40° - 150°$ angles correlates well with the pickup ion fluxes in panel (a). These ions lay outside the SWIA FOV in the fine mode. Ion mass spectra measured by STATIC is shown in panel (c). Fluxes in mass ranges 0.3 - 1.8 and 1.8 - 2.5 amu correspond to protons and alpha particles, respectively. Besides the proton and relatively weaker alpha particle fluxes, there is an ion flux at around 16 amu throughout the period. The enhanced flux above this mass between 12:55:00 and 12:56:00 UTC is most likely related to O_2^+ ions. Note that at higher mass bins STATIC measurements can be highly polluted by false counts. The magnetic field components and magnitude are shown in panel (d), with two major depressions distinguished at around 12:53:41 and 12:56:49 UTC. The depressions are 17 s and 21 s long, and the magnetic field rotation across the structures is $\sim 4°$ and $12°$, respectively. MVA analysis of the magnetic field across the depressions indicates that these structures are linearly polarized, with no indication that the they are associated with a rotational discontinuity or a reconnection current layer. Proton, alpha particle, and electron densities are shown in panel (e), while panel (f) shows the temperatures of these particles. Alpha particle densities are multiplied by a factor of 10 to match the scale of other densities, while their temperatures are divided by the same factor. The alpha particle den-

sities show enhancements inside both depressions. An electron density enhancement is particular noticeable inside the second depression at 12:56:49 UTC. The solar wind proton temperature also increases significantly inside the depressions. In panel (g) we show estimates of the magnetic pressure in cyan, solar wind ion thermal pressure in orange, electron thermal pressure in black, and total pressure ($P_{tot.} = P_B + P_i + P_e$) in green. Even though there is no apparent anticorrelation between the plasma density and the magnetic field strength, nonetheless as illustrated by the green line in panel (g), the depressions are in pressure balance and could be associated with mirror mode instabilities. The main difference between these structures and the MHs in the pure solar wind is that the ion thermal pressure enhancement in the former is caused by increased proton temperature, while in the latter, it is due to increased proton density. In panel (h) of Figure 10 we show that the solar wind bulk flow velocity inside the holes increases from the ambient solar wind. Plasma βs and temperature anisotropies for both protons and alpha particles are greater than unity during this time. The plasma βs are $\sim$1.5 and only increase to above 10 inside the depressions. In addition, the ion energy spectrogram in panel (a) shows enhanced fluxes of suprathermal ions at around 2 - 3 keV inside the depressions (yellow spots between the dashed lines). These ions enter the SWIA FOV at slightly different angles than the solar wind signal and are also seen by STATIC in the same mass range as protons. At this point, it is not clear how these ions have been accelerated to such high energies; however, the following sources could contribute to this population, (1) pickup hydrogen ions accelerated by the motional electric field, (2) solar wind protons reflected by an electric field potential across the bow shock, or (3) solar wind protons trapped and energized inside the mirror bubbles.

5 Conclusions and Implications

The MAVEN mission provided an opportunity to study various solar wind structures at 1.5 AU. Our analysis of magnetic holes/depressions in the upstream region of Mars shows that these structures have similar shape and distributions to MHs at 1 AU. At 1.5 AU, the typical linear MH structure is asymmetrical and stretched along the magnetic field with major to minor axis ratio of $\sim$1.67, which is about 10 percent smaller than the ratio at 1 AU (Xiao et al., 2010). The proton distributions inside the holes are anisotropic compared to the surrounding solar wind and the electron temperatures inside the holes show a positive correlation with the depth of the depressions. We find an

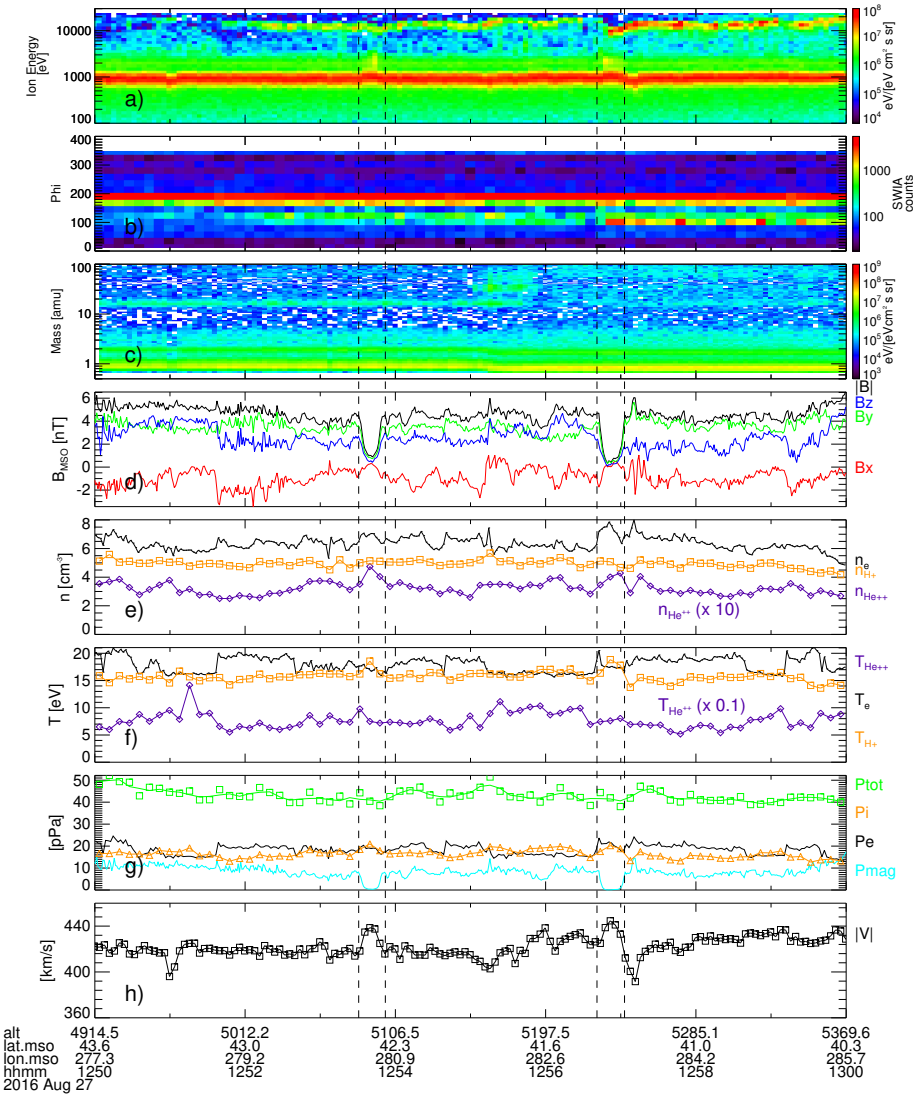

Figure 10. Magnetic hole events on 27 August 2016 accompanied by a population of heavy pickup ions. Panels show: (a) ion energy spectrogram, (b) SWIA azimuthal FOV coverage, (c) ion mass spectra measurements from STATIC (d) magnetic field components and magnitude in the MSO frame, (e) proton, alpha, and electron densities, (f) proton, alpha, and electron temperatures, (g) plasma pressure components, and (h) solar wind bulk flow speed. Alpha particle densities in panel (e) are enhanced by a factor of 10 while the temperatures in panel (f) are scaled down by a similar factor. The vertical dashed lines show the boundaries of two MHs.

occurrence rate of 2.1 events per day in MAVEN data using the selection criteria described in section 3. MAVEN observations reveal that linear MHs can be observed as part of a train of holes or as isolated single events. For MH trains, the solar wind plasma is un-

stable to mirror mode waves throughout the entire series, while isolated MHs are observed within mirror mode stable plasma, where the instability parameter R only reaches values higher than the unity inside the depression. In other words, the solar wind plasma around isolated MHs could be stable outside the depression and only becomes unstable or marginally stable when the magnetic field is reduced significantly. We presented a case study of pressure-balanced linear MHs in the solar wind carrying considerable fluxes of heavy pickup ions. Data indicate that the enhancement of ion thermal pressure inside these holes is caused by an increased proton temperature, whereas for MHs in the pure solar wind the enhancement is associated with an increased plasma density (protons in particular).

Pickup ions introduce significant temperature anisotropy to the plasma. Besides the mirror instability, temperature anisotropy can initiate another instability mode known as the ion cyclotron instability (Gary, 1992). These two modes are in competition for the available free energy of anisotropy. While the ion cyclotron mode has a higher growth rate, in the presence of heavy ions (e.g., alpha particles,) the ion cyclotron growth rate will be suppressed significantly in favor of the mirror mode (Price et al., 1986). The MHs discussed in Figure 10 are most likely associated with mirror mode structures. It is yet to be determined whether these holes have been carried by the solar wind from smaller heliocentric distances or if they have been formed farther upstream of Mars as a result of temperature anisotropy introduced by pickup ions, and then carried to the point of observation by the solar wind. We shall compare the structure scale size for two cases, (1) a sub-interval of the mirror mode structures in the pure solar wind as shown in Figure 8, and (2) a sub-interval of the structures in Figure 10 for the solar wind carrying pickup ions. The total power spectral density in the lower frequency range for each case is determined from the Morlet wavelet transform of the three components of the magnetic field. The frequency at which spectral peaks are identified in association with the mirror mode structures are found at 0.027 Hz and 0.019 Hz corresponding to wave periods of 37 s and 52 s, respectively. Using the solar wind bulk flow velocity and the background magnetic field, we find the mirror mode structure size of $\sim 49\ r_\rho$ for case 1, and $\sim 1.5\ r_{O^+}$ for case 2. We note that in case 2 the O^+ local pickup ion gyroradius is used for scaling. The scale size would be $\sim 10.8\ r_\rho$ if the enhanced proton temperatures were used instead. The mirror mode structure in case 1 is much larger than the local ion gyroradius, and most likely not formed locally but carried by the solar wind from another

location. The results suggest that the structures in case 2 on 27 August could have been formed locally upstream of Mars by the heavy pickup ions. It is worth noting that similar scale size ratios have been reported for mirror mode structures formed by water group pickup ions upstream of comets (Schmid et al., 2014; Volwerk et al., 2016). In Table 1 corresponding sub-intervals of the identified mirror mode structures with the associated period, solar wind conditions, gyroradius, and scale size are given.

Table 1. Identified mirror mode structure time spans with the associated period, solar wind conditions, ion gyroradius, and scale size

	July 25th	August 27th
Time interval	12:36:00 - 12:37:30	12:56:40 - 12:57:08
Mirror mode frequency (Hz)	0.027	0.019
SW velocity (km/s)	403	439.1
B_{bg} (nT)	1.3	4.9
Ion temperature (eV)	6 (H^+)	1.275×10^4 (O^+)
Local ion gyroradius (km)	$r_\rho = 273.2$	$r_{O^+} = 1.469 \times 10^4$
Mirror mode size	49.3 r_ρ	1.5 r_{O^+}

MAVEN orbit did not extend far beyond the bow shock (the maximum distance from the bow shock was 1.2 R_M) and we were unable to study the evolution of MHs as they approach the bow shock. However, these structures will interact with the bow shock and propagate downstream into the magnetosheath. Plasma within MHs has a higher momentum than the ambient solar wind plasma and as they interact with the bow shock, the shock front is displaced and the inner plasma configurations of the holes also change (Grib & Leora, 2015). At planets with an intrinsic magnetosphere, such as Mercury and Earth, solar wind MHs survive the bow shock and travel through the magnetosheath in the form of diamagnetic plasmoids (Karlsson et al., 2015, 2016). At comets MHs can travel to very low altitudes while their structure becomes compressed (Plaschke et al., 2018). It is plausible for solar wind MHs to change the dynamics of the Martian magnetosphere as well. The low magnetic pressure inside MHs could also disturb the pressure balance at the induced magnetospheric boundary layer. Given the high occurrence rate of MHs at Mars (at least ∼2.1 per day), any modulation of magnetospheric or ionospheric con-

ditions could have significant impacts on lower atmospheric layers in the long term. Investigations of impacts of magnetic holes on Mars' inner magnetosphere, ionospheric flows, and ion loss rates are left for a future follow up study.

Acknowledgments

All data presented in the figures are publicly available on the Planetary Data System (https://pds.nasa.gov), or can be obtained from the corresponding author. Routines for data acquisition and treatment are available through the MAVEN Toolkit publicly available on the MAVEN Science Data Center (https://lasp.colorado.edu/maven/sdc/team/pages/software.html). We acknowledge the MAVEN contract for support. Parts of this work for the observations obtained with the SWEA instrument is supported by the French space agency CNES.

References

Ahmadi, N., Germaschewski, K., & Raeder, J. (2017, December). Simulation of magnetic holes formation in the magnetosheath. *Physics of Plasmas*, *24*(12), 122121. Retrieved 2019-05-09, from `http://aip.scitation.org/doi/10.1063/1.5003017` doi: 10.1063/1.5003017

Ala-Lahti, M. M., Kilpua, E. K. J., Dimmock, A. P., Osmane, A., Pulkkinen, T., & Souček, J. (2018, May). Statistical analysis of mirror mode waves in sheath regions driven by interplanetary coronal mass ejection. *Annales Geophysicae*, *36*(3), 793–808. Retrieved 2019-06-20, from `https://www.ann-geophys.net/36/793/2018/` doi: 10.5194/angeo-36-793-2018

Balikhin, M. A., Pokhotelov, O. A., Walker, S. N., Boynton, R. J., & Beloff, N. (2010, March). Mirror mode peaks: THEMIS observations versus theories: MIRROR MODES PEAKS. *Geophysical Research Letters*, *37*(5), n/a–n/a. Retrieved 2019-07-23, from `http://doi.wiley.com/10.1029/2009GL042090` doi: 10.1029/2009GL042090

Balikhin, M. A., Sibeck, D. G., Runov, A., & Walker, S. N. (2012, August). Magnetic holes in the vicinity of dipolarization fronts: Mirror or tearing structures?: DIPOLARIZATION MAGNETIC HOLES. *Journal of Geophysical Research: Space Physics*, *117*(A8), n/a–n/a. Retrieved 2019-07-23, from `http://doi.wiley.com/10.1029/2012JA017552` doi: 10.1029/2012JA017552

Baumgärtel, K. (1999, December). Soliton approach to magnetic holes. *Journal of*

Geophysical Research: Space Physics, *104*(A12), 28295–28308. Retrieved 2019-05-09, from http://doi.wiley.com/10.1029/1999JA900393 doi: 10.1029/1999JA900393

Brain, D. A., Bagenal, F., Ma, Y.-J., Nilsson, H., & Stenberg Wieser, G. (2016, December). Atmospheric escape from unmagnetized bodies: Atmospheric Escape: Unmagnetized Bodies. *Journal of Geophysical Research: Planets*, *121*(12), 2364–2385. Retrieved 2019-06-27, from http://doi.wiley.com/10.1002/2016JE005162 doi: 10.1002/2016JE005162

Briand, C., Soucek, J., Henri, P., & Mangeney, A. (2010, December). Waves at the electron plasma frequency associated with solar wind magnetic holes: STEREO/Cluster observations: PLASMA WAVES IN MAGNETIC HOLES. *Journal of Geophysical Research: Space Physics*, *115*(A12), n/a–n/a. Retrieved 2019-05-21, from http://doi.wiley.com/10.1029/2010JA015849 doi: 10.1029/2010JA015849

Burlaga, L. F., & Lemaire, J. F. (1978). Interplanetary magnetic holes: Theory. *Journal of Geophysical Research: Space Physics*, *83*(A11), 5157–5160. Retrieved 2019-05-09, from https://agupubs.onlinelibrary.wiley.com/doi/abs/10.1029/JA083iA11p05157 doi: 10.1029/JA083iA11p05157

Burlaga, L. F., Ness, N. F., & Acuna, M. H. (2007, July). Linear magnetic holes in a unipolar region of the heliosheath observed by Voyager 1: HELIOSHEATH MAGNETIC HOLES. *Journal of Geophysical Research: Space Physics*, *112*(A7), n/a–n/a. Retrieved 2019-05-17, from http://doi.wiley.com/10.1029/2007JA012292 doi: 10.1029/2007JA012292

Burlaga, L. F., Ness, N. F., & Acũna, M. H. (2006, November). Trains of magnetic holes and magnetic humps in the heliosheath. *Geophysical Research Letters*, *33*(21). Retrieved 2019-05-03, from http://doi.wiley.com/10.1029/2006GL027276 doi: 10.1029/2006GL027276

Buti, B., Tsurutani, B. T., Neugebauer, M., & Goldstein, B. E. (2001, April). Generation mechanism for magnetic holes in the solar wind. *Geophysical Research Letters*, *28*(7), 1355–1358. Retrieved 2019-05-09, from http://doi.wiley.com/10.1029/2000GL012592 doi: 10.1029/2000GL012592

Califano, F., Hellinger, P., Kuznetsov, E., Passot, T., Sulem, P. L., & Trávníček, P. M. (2008, August). Nonlinear mirror mode dynamics: Simulations and

modeling: NONLINEAR MIRROR MODES. *Journal of Geophysical Research: Space Physics*, *113*(A8), n/a–n/a. Retrieved 2019-05-10, from http://doi.wiley.com/10.1029/2007JA012898 doi: 10.1029/2007JA012898

Chisham, G., Schwartz, S. J., Burgess, D., Bale, S. D., Dunlop, M. W., & Russell, C. T. (2000, February). Multisatellite observations of large magnetic depressions in the solar wind. *Journal of Geophysical Research: Space Physics*, *105*(A2), 2325–2335. Retrieved 2019-05-20, from http://doi.wiley.com/10.1029/1999JA900446 doi: 10.1029/1999JA900446

Collinson, G., Halekas, J., Grebowsky, J., Connerney, J., Mitchell, D., Espley, J., ... Jakosky, B. (2015, November). A hot flow anomaly at Mars: A HOT FLOW ANOMALY AT MARS. *Geophysical Research Letters*, *42*(21), 9121–9127. Retrieved 2019-06-04, from http://doi.wiley.com/10.1002/2015GL065079 doi: 10.1002/2015GL065079

Collinson, G., Sibeck, D., Omidi, N., Grebowsky, J., Halekas, J., Mitchell, D., ... Jakosky, B. (2017, October). Spontaneous hot flow anomalies at Mars and Venus. *Journal of Geophysical Research: Space Physics*, *122*(10), 9910–9923. Retrieved 2019-06-04, from https://onlinelibrary.wiley.com/doi/abs/10.1002/2017JA024196 doi: 10.1002/2017JA024196

Connerney, J. E. P., Espley, J., Lawton, P., Murphy, S., Odom, J., Oliversen, R., & Sheppard, D. (2015, December). The MAVEN Magnetic Field Investigation. *Space Science Reviews*, *195*(1-4), 257–291. Retrieved 2019-05-15, from http://link.springer.com/10.1007/s11214-015-0169-4 doi: 10.1007/s11214-015-0169-4

Erdős, G., & Balogh, A. (1996, January). Statistical properties of mirror mode structures observed by Ulysses in the magnetosheath of Jupiter. *Journal of Geophysical Research: Space Physics*, *101*(A1), 1–12. Retrieved 2019-05-03, from http://doi.wiley.com/10.1029/95JA02207 doi: 10.1029/95JA02207

Fitzenreiter, R. J., & Burlaga, L. F. (1978). Structure of current sheets in magnetic holes at 1 AU. *Journal of Geophysical Research: Space Physics*, *83*(A12), 5579–5585. Retrieved 2019-05-09, from https://agupubs.onlinelibrary.wiley.com/doi/abs/10.1029/JA083iA12p05579 doi: 10.1029/JA083iA12p05579

Fränz, M., Burgess, D., & Horbury, T. S. (2000, June). Magnetic field depressions

in the solar wind. *Journal of Geophysical Research: Space Physics*, *105*(A6), 12725–12732. Retrieved 2019-05-03, from http://doi.wiley.com/10.1029/2000JA900026 doi: 10.1029/2000JA900026

Gary, S. P. (1992). The mirror and ion cyclotron anisotropy instabilities. *Journal of Geophysical Research*, *97*(A6), 8519. Retrieved 2019-06-04, from http://doi.wiley.com/10.1029/92JA00299 doi: 10.1029/92JA00299

Gary, S. P. (1993). *Theory of space plasma microinstabilities*. Cambridge: Cambridge University Press. Retrieved 2019-07-15, from http://ebooks.cambridge.org/ref/id/CBO9780511551512 doi: 10.1017/CBO9780511551512

Gary, S. P., Gosling, J. T., & Forslund, D. W. (1981). The electromagnetic ion beam instability upstream of the Earth's bow shock. *Journal of Geophysical Research*, *86*(A8), 6691. Retrieved 2019-07-15, from http://doi.wiley.com/10.1029/JA086iA08p06691 doi: 10.1029/JA086iA08p06691

Glassmeier, K. H., Motschmann, U., Mazelle, C., Neubauer, F. M., Sauer, K., Fuselier, S. A., & Acuña, M. H. (1993). Mirror Modes and Fast Magnetoacoustic Waves Near the Magnetic Pileup Boundary of Comet P/Halley. *Journal of Geophysical Research*, *98*(A12), 20955–20964. Retrieved 2019-07-15, from http://doi.wiley.com/10.1029/93JA02582 doi: 10.1029/93JA02582

Grib, S. A., & Leora, S. N. (2015, March). The magnetic hole as plasma inhomogeneity in the solar wind and related interplanetary medium perturbations. *Geomagnetism and Aeronomy*, *55*(2), 158–165. Retrieved 2019-05-09, from https://doi.org/10.1134/S001679321502005X doi: 10.1134/S001679321502005X

Halekas, J. S., Brain, D. A., Luhmann, J. G., DiBraccio, G. A., Ruhunusiri, S., Harada, Y., ... Jakosky, B. M. (2017, November). Flows, Fields, and Forces in the Mars-Solar Wind Interaction: Mars-Solar Wind Interaction. *Journal of Geophysical Research: Space Physics*, *122*(11), 11,320–11,341. Retrieved 2019-06-04, from http://doi.wiley.com/10.1002/2017JA024772 doi: 10.1002/2017JA024772

Halekas, J. S., Ruhunusiri, S., Harada, Y., Collinson, G., Mitchell, D. L., Mazelle, C., ... Jakosky, B. M. (2017, January). Structure, dynamics, and seasonal variability of the Marssolar wind interaction: MAVEN Solar Wind

Ion Analyzer inflight performance and science results. *Journal of Geophysical Research: Space Physics*, *122*(1), 547–578. Retrieved 2019-06-04, from https://onlinelibrary.wiley.com/doi/abs/10.1002/2016JA023167 doi: 10.1002/2016JA023167

Halekas, J. S., Taylor, E. R., Dalton, G., Johnson, G., Curtis, D. W., McFadden, J. P., ... Jakosky, B. M. (2015, December). The Solar Wind Ion Analyzer for MAVEN. *Space Science Reviews*, *195*(1-4), 125–151. Retrieved 2019-06-04, from http://link.springer.com/10.1007/s11214-013-0029-z doi: 10.1007/s11214-013-0029-z

Hasegawa, A. (1969). Drift Mirror Instability in the Magnetosphere. *Physics of Fluids*, *12*(12), 2642. Retrieved 2019-06-04, from https://aip.scitation.org/doi/10.1063/1.1692407 doi: 10.1063/1.1692407

Hellinger, P., Kuznetsov, E. A., Passot, T., Sulem, P. L., & Trávníček, P. M. (2009, March). Mirror instability: From quasi-linear diffusion to coherent structures. *Geophysical Research Letters*, *36*(6). Retrieved 2019-07-15, from http://doi.wiley.com/10.1029/2008GL036805 doi: 10.1029/2008GL036805

Hoppe, M. M., & Russell, C. T. (1983). Plasma rest frame frequencies and polarizations of the low-frequency upstream waves: ISEE 1 and 2 Observations. *Journal of Geophysical Research*, *88*(A3), 2021. Retrieved 2019-07-15, from http://doi.wiley.com/10.1029/JA088iA03p02021 doi: 10.1029/JA088iA03p02021

Hubert, D., & Harvey, C. C. (2000, October). Interplanetary rotational discontinuities: From the solar wind to the magnetosphere through the magnetosheath. *Geophysical Research Letters*, *27*(19), 3149–3152. Retrieved 2019-05-10, from http://doi.wiley.com/10.1029/2000GL003776 doi: 10.1029/2000GL003776

Jakosky, B. M., Lin, R. P., Grebowsky, J. M., Luhmann, J. G., Mitchell, D. F., Beutelschies, G., ... Zurek, R. (2015, December). The Mars Atmosphere and Volatile Evolution (MAVEN) Mission. *Space Science Reviews*, *195*(1-4), 3–48. Retrieved 2019-06-04, from http://link.springer.com/10.1007/s11214-015-0139-x doi: 10.1007/s11214-015-0139-x

Joy, S. P., Kivelson, M. G., Walker, R. J., Khurana, K. K., Russell, C. T., & Paterson, W. R. (2006, December). Mirror mode structures in the Jovian

magnetosheath. *Journal of Geophysical Research*, *111*(A12). Retrieved 2019-05-03, from http://doi.wiley.com/10.1029/2006JA011985 doi: 10.1029/2006JA011985

Karlsson, T., Kullen, A., Liljeblad, E., Brenning, N., Nilsson, H., Gunell, H., & Hamrin, M. (2015, September). On the origin of magnetosheath plasmoids and their relation to magnetosheath jets: ON THE ORIGIN OF MAGNETOSHEATH PLASMOIDS. *Journal of Geophysical Research: Space Physics*, *120*(9), 7390–7403. Retrieved 2019-06-04, from http://doi.wiley.com/10.1002/2015JA021487 doi: 10.1002/2015JA021487

Karlsson, T., Liljeblad, E., Kullen, A., Raines, J. M., Slavin, J. A., & Sundberg, T. (2016, September). Isolated magnetic field structures in Mercury's magnetosheath as possible analogues for terrestrial magnetosheath plasmoids and jets. *Planetary and Space Science*, *129*, 61–73. Retrieved 2019-05-03, from https://linkinghub.elsevier.com/retrieve/pii/S0032063316300307 doi: 10.1016/j.pss.2016.06.002

Kivelson, M. G., & Southwood, D. J. (1996, August). Mirror instability II: The mechanism of nonlinear saturation. *Journal of Geophysical Research: Space Physics*, *101*(A8), 17365–17371. Retrieved 2019-05-03, from http://doi.wiley.com/10.1029/96JA01407 doi: 10.1029/96JA01407

Lammer, H., Kasting, J. F., Chassefière, E., Johnson, R. E., Kulikov, Y. N., & Tian, F. (2008, August). Atmospheric Escape and Evolution of Terrestrial Planets and Satellites. *Space Science Reviews*, *139*(1-4), 399–436. Retrieved 2019-06-22, from http://link.springer.com/10.1007/s11214-008-9413-5 doi: 10.1007/s11214-008-9413-5

Lemaire, J., & Burlaga, L. F. (1976, December). Diamagnetic boundary layers: A kinetic theory. *Astrophysics and Space Science*, *45*(2), 303–325. Retrieved 2019-05-09, from https://doi.org/10.1007/BF00642667 doi: 10.1007/BF00642667

Liu, Y., Richardson, J. D., Belcher, J. W., & Kasper, J. C. (2007, April). Temperature Anisotropy in a Shocked Plasma: Mirror-Mode Instabilities in the Heliosheath. *The Astrophysical Journal*, *659*(1), L65–L68. Retrieved 2019-05-03, from http://stacks.iop.org/1538-4357/659/i=1/a=L65 doi: 10.1086/516568

Lucek, E. A., Dunlop, M. W., Horbury, T. S., Balogh, A., Brown, P., Cargill, P., ... Oddy, T. (2001). Cluster magnetic field observations in the magnetosheath: four-point measurements of mirror structures. *Annales Geophysicae*, *19*(10/12), 1421–1428. Retrieved 2019-06-04, from http://www.ann-geophys.net/19/1421/2001/ doi: 10.5194/angeo-19-1421-2001

Mazelle, C., Belmont, G., Glassmeier, K.-H., Le Quéau, D., & Rème, H. (1991, January). Ultra low frequency waves at the magnetic pile-up boundary of comet P/Halley. *Advances in Space Research*, *11*(9), 73–77. Retrieved 2019-07-15, from https://linkinghub.elsevier.com/retrieve/pii/027311779190014B doi: 10.1016/0273-1177(91)90014-B

McFadden, J. P., Kortmann, O., Curtis, D., Dalton, G., Johnson, G., Abiad, R., ... Jakosky, B. (2015, December). MAVEN SupraThermal and Thermal Ion Compostion (STATIC) Instrument. *Space Science Reviews*, *195*(1-4), 199–256. Retrieved 2019-05-15, from http://link.springer.com/10.1007/s11214-015-0175-6 doi: 10.1007/s11214-015-0175-6

Mitchell, D. L., Mazelle, C., Sauvaud, J.-A., Thocaven, J.-J., Rouzaud, J., Fedorov, A., ... Jakosky, B. M. (2016, April). The MAVEN Solar Wind Electron Analyzer. *Space Science Reviews*, *200*(1-4), 495–528. Retrieved 2019-05-15, from http://link.springer.com/10.1007/s11214-015-0232-1 doi: 10.1007/s11214-015-0232-1

Neugebauer, M., Goldstein, B. E., Winterhalter, D., Smith, E. J., MacDowall, R. J., & Gary, S. P. (2001, April). Ion distributions in large magnetic holes in the fast solar wind. *Journal of Geophysical Research: Space Physics*, *106*(A4), 5635–5648. Retrieved 2019-05-28, from http://doi.wiley.com/10.1029/2000JA000331 doi: 10.1029/2000JA000331

Omidi, N., & Sibeck, D. G. (2007, January). Formation of hot flow anomalies and solitary shocks: HFAS AND SOLITARY SHOCKS. *Journal of Geophysical Research: Space Physics*, *112*(A1), n/a–n/a. Retrieved 2019-06-04, from http://doi.wiley.com/10.1029/2006JA011663 doi: 10.1029/2006JA011663

Omidi, N., Sibeck, D. G., & Blanco-Cano, X. (2009, August). Foreshock compressional boundary: FORESHOCK COMPRESSIONAL BOUNDARY. *Journal of Geophysical Research: Space Physics*, *114*(A8), n/a–n/a. Retrieved 2019-06-06, from http://doi.wiley.com/10.1029/2008JA013950 doi:

10.1029/2008JA013950

Omidi, N., Zhang, H., Sibeck, D., & Turner, D. (2013, January). Spontaneous hot flow anomalies at quasi-parallel shocks: 2. Hybrid simulations: HYBRID SIMULATIONS OF SHFAS. *Journal of Geophysical Research: Space Physics*, *118*(1), 173–180. Retrieved 2019-06-04, from http://doi.wiley.com/10.1029/2012JA018099 doi: 10.1029/2012JA018099

Plaschke, F., Karlsson, T., Götz, C., Möstl, C., Richter, I., Volwerk, M., ... Goldstein, R. (2018, October). First observations of magnetic holes deep within the coma of a comet. *Astronomy & Astrophysics*, *618*, A114. Retrieved 2019-05-03, from https://www.aanda.org/10.1051/0004-6361/201833300 doi: 10.1051/0004-6361/201833300

Pokhotelov, O. A. (2002). Linear theory of the mirror instability in non-Maxwellian space plasmas. *Journal of Geophysical Research*, *107*(A10). Retrieved 2019-07-18, from http://doi.wiley.com/10.1029/2001JA009125 doi: 10.1029/2001JA009125

Price, C. P., Swift, D. W., & Lee, L.-C. (1986). Numerical simulation of nonoscillatory mirror waves at the Earth's magnetosheath. *Journal of Geophysical Research*, *91*(A1), 101. Retrieved 2019-06-02, from http://doi.wiley.com/10.1029/JA091iA01p00101 doi: 10.1029/JA091iA01p00101

Russell, C. T., Jian, L. K., Luhmann, J. G., Zhang, T. L., Neubauer, F. M., Skoug, R. M., ... Cowee, M. M. (2008, August). Mirror mode waves: Messengers from the coronal heating region. *Geophysical Research Letters*, *35*(15). Retrieved 2019-06-06, from http://doi.wiley.com/10.1029/2008GL034096 doi: 10.1029/2008GL034096

Russell, C. T., Riedler, W., Schwingenschuh, K., & Yeroshenko, Y. (1987, June). Mirror instability in the magnetosphere of comet Halley. *Geophysical Research Letters*, *14*(6), 644–647. Retrieved 2019-05-09, from http://doi.wiley.com/10.1029/GL014i006p00644 doi: 10.1029/GL014i006p00644

Schmid, D., Volwerk, M., Plaschke, F., Vörös, Z., Zhang, T. L., Baumjohann, W., & Narita, Y. (2014, June). Mirror mode structures near Venus and Comet P/Halley. *Annales Geophysicae*, *32*(6), 651–657. Retrieved 2019-06-25, from https://www.ann-geophys.net/32/651/2014/ doi: 10.5194/angeo-32-651-2014

Schwartz, S. J., & Burgess, D. (1991, March). Quasi-parallel shocks: A patchwork of three-dimensional structures. *Geophysical Research Letters*, *18*(3), 373–376. Retrieved 2019-06-06, from http://doi.wiley.com/10.1029/91GL00138 doi: 10.1029/91GL00138

Schwartz, S. J., Sibeck, D., Wilber, M., Meziane, K., & Horbury, T. S. (2006). Kinetic aspects of foreshock cavities. *Geophysical Research Letters*, *33*(12). Retrieved 2019-06-02, from http://doi.wiley.com/10.1029/2005GL025612 doi: 10.1029/2005GL025612

Sibeck, D. G., Kudela, K., Mukai, T., Nemecek, Z., & Safrankova, J. (2004, December). Radial dependence of foreshock cavities: a case study. *Annales Geophysicae*, *22*(12), 4143–4151. Retrieved 2019-06-02, from http://www.ann-geophys.net/22/4143/2004/ doi: 10.5194/angeo-22-4143-2004

Smith, E. J. (1973, May). Identification of interplanetary tangential and rotational discontinuities. *Journal of Geophysical Research*, *78*(13), 2054–2063. Retrieved 2019-05-20, from http://doi.wiley.com/10.1029/JA078i013p02054 doi: 10.1029/JA078i013p02054

Soucek, J., Lucek, E., & Dandouras, I. (2008, April). Properties of magnetosheath mirror modes observed by Cluster and their response to changes in plasma parameters: MIRROR MODE PROPERTIES. *Journal of Geophysical Research: Space Physics*, *113*(A4), n/a–n/a. Retrieved 2019-05-03, from http://doi.wiley.com/10.1029/2007JA012649 doi: 10.1029/2007JA012649

Southwood, D. J., & Kivelson, M. G. (1993). Mirror instability: 1. Physical mechanism of linear instability. *Journal of Geophysical Research*, *98*(A6), 9181. Retrieved 2019-05-28, from http://doi.wiley.com/10.1029/92JA02837 doi: 10.1029/92JA02837

Sperveslage, K., Neubauer, F. M., Baumgärtel, K., & Ness, N. F. (2000). Magnetic holes in the solar wind between 0.3 AU and 17 AU. *Nonlinear Processes in Geophysics*, *7*(3/4), 191–200. Retrieved 2019-06-04, from http://www.nonlin-processes-geophys.net/7/191/2000/ doi: 10.5194/npg-7-191-2000

Stevens, M. L., & Kasper, J. C. (2007, May). A scale-free analysis of magnetic holes at 1 AU: MAGNETIC HOLES AT 1 AU. *Journal of Geophysical Research: Space Physics*, *112*(A5), n/a–n/a. Retrieved 2019-05-03, from http://

doi.wiley.com/10.1029/2006JA012116 doi: 10.1029/2006JA012116

Szegö, K., Glassmeier, K.-H., Bingham, R., Bogdanov, A., Fischer, C., Haerendel, G., ... Zank, G. (2000, December). Physics of Mass Loaded Plasmas. *Space Science Reviews*, *94*(3), 429–671. Retrieved 2018-09-08, from https://doi.org/10.1023/A:1026568530975 doi: 10.1023/A:1026568530975

Tajiri, M. (1967, June). Propagation of Hydromagnetic Waves in Collisionless Plasma. II. Kinetic Approach. *Journal of the Physical Society of Japan*, *22*(6), 1482–1494. Retrieved 2019-06-04, from http://journals.jps.jp/doi/10.1143/JPSJ.22.1482 doi: 10.1143/JPSJ.22.1482

Trotignon, J., Mazelle, C., Bertucci, C., & Acuña, M. (2006, April). Martian shock and magnetic pile-up boundary positions and shapes determined from the Phobos 2 and Mars Global Surveyor data sets. *Planetary and Space Science*, *54*(4), 357–369. Retrieved 2019-06-04, from https://linkinghub.elsevier.com/retrieve/pii/S0032063306000110 doi: 10.1016/j.pss.2006.01.003

Tsurutani, B. T. (2002). Relationship between discontinuities, magnetic holes, magnetic decreases, and nonlinear Alfvén waves: Ulysses observations over the solar poles. *Geophysical Research Letters*, *29*(11). Retrieved 2019-05-31, from http://doi.wiley.com/10.1029/2001GL013623 doi: 10.1029/2001GL013623

Tsurutani, B. T., Dasgupta, B., Galvan, C., Neugebauer, M., Lakhina, G. S., Arballo, J. K., ... Buti, B. (2002, December). Phase-steepened Alfvén waves, proton perpendicular energization and the creation of magnetic holes and magnetic decreases: The ponderomotive force: THE PONDEROMOTIVE FORCE. *Geophysical Research Letters*, *29*(24), 86–1–86–4. Retrieved 2019-05-15, from http://doi.wiley.com/10.1029/2002GL015652 doi: 10.1029/2002GL015652

Tsurutani, B. T., Guarnieri, F. L., Echer, E., Lakhina, G. S., & Verkhoglyadova, O. P. (2009, August). Magnetic decrease formation from <1 AU to ∼5 AU: Corotating interaction region reverse shocks: MAGNETIC DECREASE FORMATION. *Journal of Geophysical Research: Space Physics*, *114*(A8), n/a–n/a. Retrieved 2019-06-04, from http://doi.wiley.com/10.1029/2008JA013927 doi: 10.1029/2008JA013927

Tsurutani, B. T., Lakhina, G. S., Verkhoglyadova, O. P., Echer, E., Guarnieri, F. L., Narita, Y., & Constantinescu, D. O. (2011, February). Magnetosheath and heliosheath mirror mode structures, interplanetary magnetic decreases, and linear magnetic decreases: Differences and distinguishing features: REVIEW. *Journal of Geophysical Research: Space Physics*, *116*(A2), n/a–n/a. Retrieved 2019-05-03, from http://doi.wiley.com/10.1029/2010JA015913 doi: 10.1029/2010JA015913

Tsurutani, B. T., Southwood, D. J., Smith, E. J., & Balogh, A. (1992, June). Nonlinear magnetosonic waves and mirror mode structures in the March 1991 Ulysses interplanetary event. *Geophysical Research Letters*, *19*(12), 1267–1270. Retrieved 2019-05-21, from http://doi.wiley.com/10.1029/92GL00782 doi: 10.1029/92GL00782

Turner, J. M., Burlaga, L. F., Ness, N. F., & Lemaire, J. F. (1977, May). Magnetic holes in the solar wind. *Journal of Geophysical Research*, *82*(13), 1921–1924. Retrieved 2019-05-03, from http://doi.wiley.com/10.1029/JA082i013p01921 doi: 10.1029/JA082i013p01921

Volwerk, M., Richter, I., Tsurutani, B., Götz, C., Altwegg, K., Broiles, T., ... Glassmeier, K.-H. (2016, January). Mass-loading, pile-up, and mirror-mode waves at comet 67p/Churyumov-Gerasimenko. *Annales Geophysicae*, *34*(1), 1–15. Retrieved 2018-02-23, from https://www.ann-geophys.net/34/1/2016/ doi: 10.5194/angeo-34-1-2016

Winterhalter, D., Neugebauer, M., Goldstein, B. E., Smith, E. J., Bame, S. J., & Balogh, A. (1994). Ulysses field and plasma observations of magnetic holes in the solar wind and their relation to mirror-mode structures. *Journal of Geophysical Research*, *99*(A12), 23371. Retrieved 2019-05-03, from http://doi.wiley.com/10.1029/94JA01977 doi: 10.1029/94JA01977

Winterhalter, D., Neugebauer, M., Goldstein, B. E., Smith, E. J., Tsurutani, B. T., Bame, S. J., & Balogh, A. (1995, April). Magnetic holes in the solar wind and their relation to mirror-mode structures. *Space Science Reviews*, *72*(1-2), 201–204. Retrieved 2019-06-04, from http://link.springer.com/10.1007/BF00768780 doi: 10.1007/BF00768780

Winterhalter, D., Smith, E. J., Neugebauer, M., Goldstein, B. E., & Tsurutani, B. T. (2000, June). The latitudinal distribution of solar wind mag-

netic holes. *Geophysical Research Letters*, *27*(11), 1615–1618. Retrieved 2019-05-03, from http://doi.wiley.com/10.1029/1999GL003717 doi: 10.1029/1999GL003717

Wu, C. S., & Davidson, R. C. (1972, October). Electromagnetic instabilities produced by neutral-particle ionization in interplanetary space. *Journal of Geophysical Research*, *77*(28), 5399–5406. Retrieved 2019-05-21, from http://doi.wiley.com/10.1029/JA077i028p05399 doi: 10.1029/JA077i028p05399

Xiao, T., Shi, Q. Q., Zhang, T. L., Fu, S. Y., Li, L., Zong, Q. G., ... Reme, H. (2010, September). Cluster-C1 observations on the geometrical structure of linear magnetic holes in the solar wind at 1 AU. *Annales Geophysicae*, *28*(9), 1695–1702. Retrieved 2019-05-03, from http://www.ann-geophys.net/28/1695/2010/ doi: 10.5194/angeo-28-1695-2010

Zhang, T. L., Russell, C. T., Baumjohann, W., Jian, L. K., Balikhin, M. A., Cao, J. B., ... Vörös, Z. (2008, May). Characteristic size and shape of the mirror mode structures in the solar wind at 0.72 AU: SOLAR WIND MIRROR MODE STRUCTURES. *Geophysical Research Letters*, *35*(10). Retrieved 2019-05-03, from http://doi.wiley.com/10.1029/2008GL033793 doi: 10.1029/2008GL033793

Zhang, T. L., Russell, C. T., Zambelli, W., Vörös, Z., Wang, C., Cao, J. B., ... Glassmeier, K.-H. (2008, December). Behavior of current sheets at directional magnetic discontinuities in the solar wind at 0.72 AU. *Geophysical Research Letters*, *35*(24). Retrieved 2019-05-03, from http://doi.wiley.com/10.1029/2008GL036120 doi: 10.1029/2008GL036120

Zurbuchen, T. H., Hefti, S., Fisk, L. A., Gloeckler, G., Schwadron, N. A., Smith, C. W., ... Burlaga, L. F. (2001). On the origin of microscale magnetic holes in the solar wind. *Journal of Geophysical Research: Space Physics*, *106*(A8), 16001–16010. Retrieved 2019-05-09, from https://agupubs.onlinelibrary.wiley.com/doi/abs/10.1029/2000JA000119 doi: 10.1029/2000JA000119